The structural and functional characterization of Malus domestica double bond reductase MdDBR provides insights towards the identification of its substrates

The structural and functional characterization of *Malus domestica* double bond reductase MdDBR provides insights towards the identification of its substrates.

Rosanna Caliandro [a], Ivan Polsinelli [a], Nicola Demitri [b], Francesco Musiani [c], Stefan Martens [d], Stefano Benini [a*]

[a] Bioorganic Chemistry and Bio-Crystallography laboratory (B_2Cl), Faculty of Science and Technology, Free University of Bolzano, Piazza Università 5, 39100 Bolzano, Italy

[b] Elettra-Sincrotrone Trieste, S.S. 14 Km 163.5 in Area Science Park, Basovizza, Trieste 34149, Italy

[c] Laboratory of Bioinorganic Chemistry, Department of Pharmacy and Biotechnology, University of Bologna, Via Giuseppe Fanin 40, 40127 Bologna, Italy

[d] Department of Food Quality and Nutrition, Centro Ricerca e Innovazione, Fondazione Edmund Mach, Via E. Mach 1, 38010 San Michele all'Adige, Trentino, Italy

*To whom the correspondence should be addressed: S. Benini; Phone: +39-0471-017128; Fax: +39-0471-017109; E-mail: stefano.benini@unibz.it.

Abstract

In this study we describe the crystal structures of the apoform, the binary and the ternary complexes of a double bond reductase from *Malus domestica* L. (MdDBR) and explore a range of potential substrates.

The overall fold of MdDBR is similar to that of the medium chain reductase/dehydrogenase/zinc-dependent alcohol dehydrogenase-like family. Structural comparison of MdDBR with *Arabidopsis thaliana* DBR (AtDBR), *Nicotiana tabacum* DBR (NtDBR) and *Rubus idaeus* DBR (RiDBR) allowed the identification of key amino acids involved in cofactor and ligands binding and shed light on how these residues may guide the orientation of the substrates.

The enzyme kinetic for the substrate trans-4-phenylbuten-2-one has been analyzed, and MdDBR activity towards a variety of substrates was tested. This enzyme has been reported to be involved in the phenylpropanoid pathway where it would catalyze the NADPH-dependent reduction of the α, β-unsaturated double bond of carbonyl metabolites. Our study provides new data towards the identification of MdDBR natural substrate and the biosynthetic pathway where it belongs. Furthermore, the originally proposed involvement in dihydrochalcone biosynthesis in apple must be questioned.

Keywords: Phenylpropanoid pathway, Apple, Double Bond Reductase, X-ray crystal structure, *α*, *β*-unsaturated double bond, NADPH-dependent reduction

1. Introduction

Phenylpropanoids are an extensive class of secondary metabolites widely distributed in the plant kingdom. They play important roles in plant structural support, being indispensable components of cell walls, in plant defense against herbivores and pathogens, in plant protection against excessive light and UV radiation, and in flower and seed pigmentation to facilitate plant fertility and reproduction [1] [2]. Phenylpropanoid derivatives have also received considerable attention for their medicinal and health protecting properties that make them excellent candidates as pharmacologically active drugs or as functional food ingredients. An example is dihydroconiferyl alcohol, shown to be a potentially useful anti-inflammatory agent [3], or phloridzin, which is accumulating mainly in *Malus* species [4], reported to be promising for the treatment of Diabetes Mellitus, obesity, and stress hyperglycemia [5].

The phenylpropanoid pathway starts with the deamination of L-phenylalanine eventually leading to the biosynthesis of phenolic acids, monolignols, flavonoids, stilbenes and coumarins [2]. Several oxidoreductases are involved in this pathway, such as phenylcoumaran benzylic ether reductase [6], cinnamyl alcohol dehydrogenase [7], secoisolariciresinol dehydrogenase [8] and alkenal double bond reductases [9] [10]. The latter catalyze the NADPH-dependent reduction of α, β-unsaturated double bonds of many secondary carbonyl metabolites. Alkenal double bond reductases (DBR, EC 1.3.1.102) have become important biotechnological tools for asymmetric synthesis because of their stereoselectivity in the C=C reduction, for example in the trans-specific reduction of activated alkenes [11]. The reduction of alkenal double bond catalysed by DBRs has been proposed to proceed through stereoselective transfer of a hydride from NADPH to the β-carbon of the reduced substrate [12] (Fig. 1). Various DBRs, involved in the phenylpropanoid pathway, have been isolated from different plant species. For example, *Pinus taeda* L. phenylpropenal DBR converts both dehydrodiconiferyl and coniferyl aldehydes into dihydrodehydrodiconiferyl and dihydroconiferyl aldehydes, respectively [13]. Its *Arabidopsis thaliana* L. homologue, *At*DBR, reduces the C7−C8 double bond of *p*-coumaryl- and coniferyl aldehydes [9]. The *Nicotiana tabacum* L. DBR has been shown to be active towards a variety of α, β-unsaturated activated alkenes [10], such as *trans*-cinnamaldehyde or 1-nitrocyclohexene. Additionally, *Rubus idaeus* L. raspberry ketone/zingerone synthase 1 catalyzes the reduction of 4-hydroxybenzalacetone and 3-methoxy-4-hydroxybenzalacetone to raspberry ketone (4-(4-Hydroxyphenyl)butan-2-one) and zingerone (4-(4-Hydroxy-3-methoxyphenyl)butan-2-one), respectively [14]. A DBR from *Malus domestica* L. has been isolated and characterized [15] and suggested to be involved in the biosynthesis of polyphenolic compounds, such as dihydrochalcones, beneficial in human diet [16].

In the present study, we report the crystal structure of *M. domestica* DBR (MdDBR), in its apo form, in complex with the cofactor $NADP^+$ and in complex with the cofactor $NADP^+$ plus ferulic acid (FER). Together with the enzymatic characterization carried out in this study we provide new insight on MdDBR substrate specificity. These results are the starting point for future structure-driven site-directed mutagenesis studies, that can be performed to expand the biocatalytic potential of this enzyme.

2. Materials and methods

2.1 Enzyme production and purification

MdDBR cDNA cloned into the pEXP5-NT/TOPO TA expression vector was transformed into BL21(DE3) *Escherichia coli* cells [15]. Transformed cells were grown in auto-inducting media [17] supplemented with 100 μg ml^{-1} Ampicillin. After an incubation of 48 h at 16 °C, cells were harvested by centrifugation at 4000*g* for 15 min at 4 °C and resuspended in buffer A (50 mM Tris–HCl buffer pH 7.5, 300 mM NaCl, 10% glycerol, 20 mM imidazole and 2 mM DTT), with 0.2 mg ml^{-1} lysozyme (Sigma Aldrich, USA) and 0.01 mg ml^{-1} DNAse. The cell suspension was sonicated for 2 min with cycles of 15 sec to disrupt the cells, followed by extract clarification by centrifugation for 30 min at 18000*g* at 4 °C. The supernatant containing the soluble recombinant MdDBR protein was applied to a 5 ml HisTrap column (GE Healthcare, Sweden) pre-equilibrated with buffer A; the protein was eluted stepwise with a gradient of buffer B (50 mM Tris–HCl buffer pH 7.5, 300 mM NaCl, 10% glycerol, 2 mM DTT and 500 mM Imidazole). The MdDBR-enriched fractions were pooled and dialyzed against buffer A to remove the excess of imidazole and then incubated with His-tagged TEV protease at a 1:10 ratio for 2 h at 20 °C to cleave the N-terminal 6xHis-tag. The protein solution was then reapplied to the 5 ml HisTrap column pre-equilibrated as before to remove the TEV protease, the cleaved 6xHis-tags and the uncleaved 6xHis-tag-MdDBR. The flow through was collected and concentrated using a Vivaspin 20 ultrafiltration unit (Sartorius, Germany) with 10,000 Da MWCO membrane to a volume of about 2 ml. The sample was run through a Superdex 200 16/60 column (GE Healthcare, Sweden) equilibrated with buffer C (20 mM Tris-HCl buffer pH 8, 300 mM NaCl, 1 mM DTT and 1 mM EDTA) and the MdDBR peak was collected. Recombinant protein purity and the estimated molecular mass of 38 kDa were assessed by SDS-PAGE.

2.2. Crystallization and data collection

The purified MdDBR was concentrated and buffer exchanged using a Vivaspin 20 ultrafiltration unit to a final concentration of 30 mg/ml in 20 mM Tris-HCl buffer pH 8, 1 mM EDTA, 1 mM DTT and 150 mM NaCl (buffer D). Protein concentration was determined by direct UV measurement at 280 mm on a DS-11 Series Spectrophotometer (Denovix) (ε = 42,290 M^{-1} cm^{-1} calculated by ProtParam, ExPASy [18]). Crystallization conditions were screened with a range of commercially available kits, CSSI and CSSII, JCSG and MORPHEUS I (Molecular Dimensions, UK), using a microbatch under-oil method in 96-well MRC plates (Molecular Dimensions, UK); each well contained 15 μl volatile oil (MDs-06, Molecular Dimensions, UK) where 1 μl of precipitant solution was mixed with 1 μl of protein solution and incubated at 20 °C. Apo-MdDBR crystals were observed in several conditions within 3 days. Based on crystal size and shape, a few of these conditions were optimized by hanging-drop vapor-diffusion, using 1 μl of protein solution with an equal volume of precipitant solution and equilibrated against 300 μl reservoir in MRC plates (Hampton Research, CA, USA). Crystals used in data collections grew within 3-4 days using a reservoir containing 12.5% (w/v) PEG 1000, 12.5% (w/v) PEG 3350, 12.5% (w/v) MPD, 0.03 M magnesium chloride, 0.03 M calcium chloride, 0.03 M sodium chloride, 0.03 M sodium bromide, 0.03 M sodium

iodide in 0.1 M MES/imidazole pH 6.5. The binary complex (MdDBR + $NADP^+$) crystals were obtained under the same conditions with the addition of 5 mM $NADP^+$ in the reservoir. As for this complex, the ternary complex (MdDBR + $NADP^+$ + FER) crystals were obtained by cocrystallization under the same conditions with an addition of 5 mM $NADP^+$ and 5 mM ferulic acid to the reservoir. Crystals were harvested using cryoloops (Hampton Research, USA) and flash-frozen in liquid nitrogen with cryoprotection provided by the crystallization condition.

2.3. Data collection, structure solution and refinement

Data for the apo form, the binary complex, and the ternary complex were collected at XRD1 (apoform and binary complex) and XRD2 (ternary complex) beamlines of the Elettra Synchrotron Trieste (Italy) [19] using a Pilatus 2M (XRD1 beamline) and Pilatus 6M (XRD2 beamline) hybrid-pixel area detectors (Dectris, CH) at 100 K and a wavelength of 1.00 Å (Table 1). Data processing was done with XDS [20] and the CCP4 package was used for model building, refinement and analysis [21]. The coordinates of DBR from *A. thaliana* (AtDBR; PDB code 2J3H) were used to solve the structure of MdDBR apoform (apo-MdDBR) by molecular replacement with MOLREP [22]. Apo-MdDBR was used as a starting model for building the structures of the binary and ternary complex. The high-resolution data allowed anisotropic refinement of the structures with REFMAC5 [23] with alternate rounds of manual model rebuilding and water addition in COOT [24]. The atomic coordinates and structure factors of apo form, $NADP^+$ bound form and $NADP^+$-FER bound form of MdDBR have been deposited in the Protein Data Bank (PDB) under the accession codes 6YSB, 6YTZ and 6YUX, respectively. The interactions involved in the dimeric interfaces were analyzed by the protein interfaces, surfaces, and assemblies service PISA at the European Bioinformatics Institute (https://www.ebi.ac.uk/pdbe/pisa/pistart.html). Crystallographic figures were created using PyMOL (The PyMOL Molecular Graphics System, Version 2.20 Schroedinger, LLC.). A summary of data collection and refinement statistics is reported in Table 1.

2.4 Enzymatic assays

Steady-state kinetic analysis were performed in 0.1 mM MES buffer pH 6.5 using trans-4-phenylbuten-2-one **(a)** (Sigma-Aldrich, ≥ 99%) as a substrate (0, 20, 50, 100, 200 µM), 1 mM NADPH and 0.4 µM MdDBR in a total volume of 1 ml. Reactions were followed continuously by monitoring NADPH oxidation at 365 nm (ε_{365} = 2561 M^{-1} cm^{-1}) for 1 min at 30 °C on a Cary UV-50 Bio UV/VIS spectrophotometer (Agilent Technologies) using a polystyrene cuvette (1 mL; Sarstedt) with a 1 cm path length. Lineweaver–Burk plots were used to determine the Michaelis–Menten constant (K_m), maximum velocity (V_{max}) and turnover number (K_{cat}). All calculations were performed using Microsoft Excel.

The conversion of 4-hydroxybenzalacetone **(b)**, 3-methoxy-4-hydroxy-benzalacetone **(c)**, coumaric acid **(d)**, ferulic acid **(e)** and *p*-coumaroyl aldehyde **(f)** with MdDBR was performed in the same conditions in a total volume of 250 µl, but in this case the reaction was stopped after 45 min by adding 200 µl ethyl acetate and the reduced product formation was checked by UPLC-DAD analysis.

When *p*-coumaroyl CoA **(g)** and feruloyl CoA **(h)** were used as candidate substrates, three different buffer conditions were tested: 50 mM Tris-HCl buffer pH 7.5; 2.5 mM citrate-phosphate buffer pH 5 and 0.1 mM MES

buffer pH 6.5, with 2 mM substrate, 2 mM NADPH and 0.4 µM MdDBR with or without His-tag, in each condition reactions were carried out for 45 min at both 30 or 35 °C and then stopped by the addition of 11.2 µl 5 N NaOH. After the hydrolysis of the CoA-esters at 45 °C for 45 min, the mixtures were neutralized by the addition of 12.4 µl 6 N HCl and extracted twice with 200 µl ethyl acetate. The combined organic phases were evaporated using a SpeedVac and resuspended in 50 µl 80 % methanol. An aliquot (5 µl) of each assay mixture was analyzed on an Agilent UPLC-DAD 1290 Infinity system. The separation was accomplished under gradient conditions on an Acquity BEH C18 1,7 µm column (2,1x150 mm; Waters, Milano, Italy) equipped with the respective pre-column, with solvent A (0.05% formic acid in water) and solvent B (0.05% formic acid in acetonitrile). Gradient starts with 95% A to 70% A in 8 min, further to 2% A in 2 min, followed by a plateau of 2,5 min, up to 95% A in 0,1 min and final plateau of 3,4 min with flow rate of 0.35 ml/min and monitored at 222, 280 and 350 nm. Column oven was set at 45 °C. All described substrates and the expected products including CoA esters and aldehydes were obtained in HPLC purity higher than 98% from TransMIT PlantMetaChem (Giessen, Germany).

2.5 Molecular docking

The initial structure of ligands **a**-**f** were generated using UCSF Chimera [25]. The ligands were parametrized by using the GAFF force field [26] and minimized by using 1000 steps of steepest descent minimization followed by 100 steps of conjugate gradient using UCSF Chimera. The minimized structures were used to generate ligand conformers through OpenEye OMEGA [27]. Conformers with internal clashes and duplicates were discarded by the software and the remaining ones were clustered based on the root mean square deviation (RMSD). For this virtual screening, a maximum of 200 conformers per compound, clustered with a RMSD of 0.5 Å, was used. If the number of conformers generated exceeds the specified maximum, only the ones with lowest energies are retained.

The binary complex of MdDBR was pre-processed using OpenEye Make Receptor 3.5.0.4 tool. Rigid docking was then performed using OpenEye FRED 3.5.0.4 [28], which is included in the OEDocking 3.4.0.4 suite. Each conformer was docked by FRED in the negative image of the active site of the target protein, which consists of a shape potential field in the binding site volume. The highest values in this field represent points where molecules can have a high number of contacts, without clashing into the protein structure. In its exhaustive search, FRED translates and rotates the structure of each conformer within the negative image of the active site, scoring each pose. FRED's first step has a default translational and rotational resolution of 1.0 and 1.5 Å, respectively. The 100 best scoring poses were then optimized with translational and rotational single steps of 0.5 and 0.75 Å, respectively, exploring all the 729 (six degrees of freedom with three positions = 36) nearby poses. The best scoring pose was retained and assigned to the compound. The binding poses were evaluated by using the Chemgauss4 scoring function implemented in OpenEye FRED 3.5.0.4 [28]. The docked ligands were visualized and analyzed by using UCSF Chimera and scripts available in the OpenEye toolkit.

3. Results and discussion

3.1 Overall structure of MdDBR

The X-ray crystal structures of MdDBR in its apoform, and in complex with $NADP^+$ (binary complex) or $NADP^+$ and ferulic acid (ternary complex) were solved (Fig. 2A, B, C) to a maximum resolution of 1.2, 1.4 and 1.3 Å resolution, respectively. Data collection and refinement statistic of the three structures are listed in Table 1. The apo-MdDBR structure forms a crystallographic dimer (Fig. 2A) not corresponding to the biologically relevant one (Fig. S1, Table S1). In the binary and ternary complex instead, the asymmetric unit contains only one monomer (Fig. 2B, 2C). The PDBePISA server calculations and size exclusion chromatography of the protein suggest that the biologically relevant form of the enzyme is a homodimer as reported previously for other DBRs [9].

A PDBefold structure alignment analysis [29] of MdDBR on the PDB database gave as the highest match the raspberry ketone/zingerone synthase 1 (RiDBR) from *R. idaeus* with a Q-score of 0.91 and sequence identity of 83 %, followed by *N. tabacum* (Q-score of 0.91, 80 % sequence identity) and *A. thaliana* (Q-score of 0.89, 72 % sequence identity) double bond reductases (Fig. 3). All the mentioned enzymes belong to the medium chain reductase/dehydrogenase/zinc-dependent alcohol dehydrogenase-like (MDR) family [30] [31].

MdDBR shows the two typical conserved structural features of the MDR family: a C-terminal nucleotide coenzyme-binding Rossmann fold domain and an N-terminal catalytic domain. The nucleotide binding domain (residues 142-309, Fig. 3) features seven α helices and six β sheets, forming a typical six-stranded parallel β-sheet sandwiched by three helices on each side. The catalytic domain (residues 1-141 and 310-349, Fig. 3) contains three α-helices and nine β-strands forming a twisted partial β-barrel-like structure. The two domains are separated by a cleft containing a deep pocket which accommodates the cofactor and forms the active site (Fig. 2). The multiple amino acid sequence alignment (Fig. 3) shows that mostly of the conserved regions are located in the NADP(H)-binding domain.

The $2F_{obs}$-F_{calc} electron density maps obtained for the three solved crystal structures are well defined and continuous apart from two highly flexible loops. The first one is situated at the entrance of the active site cavity (residues 68 to 74), because of disorder this region could be modelled only for the binary complex (Fig. 2B). The second flexible loop is between residues 267 and 274 in the nucleotide binding domain. The electron density corresponding to $NADP^+$ is shown in Fig. 4A, the cofactor is bound in a typical conformation as in AtDBR and NtDBR [32] [10]; most of the residues that are interacting with $NADP^+$ are conserved amino acids of the nucleotide binding domain (Fig. 3, yellow bars): Lys196; Tyr 212; Asn338; Val172; Ala171 and Tyr264 establish hydrogen bonds with the phosphate groups and ribose rings of NADP(H), while all the other residues make hydrogen bonds with adjacent water molecules that are connected with NADP(H). Notably, Cys258, Phe288 and Val290 anchor the nicotinamide ring by forming hydrogen bonds with the carbonyl and the amine group (Fig. 4A).

The clearly defined electron density maps obtained for FER indicates that the ligand is oriented with its aromatic ring towards the nicotinamide ring of $NADP^+$ (Fig. 4B, Fig. S2). The B-factor values of FER are higher than those of the surrounding residues indicating that FER is relatively "free to move". On the other hand, the hydroxide substituent in C4 of FER has a much lower B-value (17.72) compared to the other atoms of the ligand (from 24.51 to

38.71), indicating that this OH-group is stabilized by the hydrogen bond with the adjacent water molecule (H_2O1). H_2O1 makes hydrogen bonds with Tyr59 and the ribosyl group of $NADP^+$. FER is at van der Waals interaction distance with Tyr264, (a conserved NADP(H)-binding residues) Leu289 and Phe291 (Fig. 4B).

3.2 Structural alignments

A superimposition of the three MdDBR structures shows an overall conservation with significant differences only in the orientation of key residues in the NADPH and FER binding pocket (Fig. 5). Interactions with $NADP^+$ causes a change in the position of Tyr264 (Cα shifting of 1.9 Å), Ala171 (Cα movement of 0.8 Å) and Lys196 (its amino group rotates of 48.7°) with a consequent shift of Tyr315 (rotation of 45° of its phenyl ring), Ile261 (Cα shifting of 0.5 Å) and Phe23 (Cα movement of 0.6 Å) compared to the apo-MdDBR. Interestingly, the orientation of Phe291 results in each structure different (Fig. 5); its Cα is moving of 0.5 Å when switching from apo form to ligands incorporating structures, furthermore between the binary and the ternary structure a rotation of 66° is observed for its aromatic ring. It is possible that this is the result of the hydrophobic contact between Phe291 and the methoxy group of FER.

We compared the ternary complex structure of MdDBR with the ternary complex structures of the DBRs with the highest degree of structural similarity (NtDBR, AtDBR, RiDBR). Their superimposition (Fig. 6) shows that the ligands adopt a different orientation in each structure. Moreover, the compared proteins show significant differences in key residues in the active site [32] [10] [14]; whereas the three tyrosine of the cleft are conserved in all the structures, Phe291 of MdDBR and RiDBR and Phe285 of NtDBR are substituted by Ser287 in AtDBR. Furthermore, Leu289 of MdDBR and Leu283 of NtDBR are replaced by a Val285 in AtDBR and a Met289 in RiDBR. These different residues are most likely the cause of the dissimilar ligand orientations in the various structures. Comparing the binding site surfaces in AtDBR and MdDBR (Fig. 7A and 7B, respectively), it is important to notice, that the presence of phenylalanine (Phe291) and leucine (Leu289) in MdDBR instead of serine (Ser287) and valine (Val285), as in AtDBR, clearly results in a steric hindrance that prevents positioning of the disubstituted ring of the substrate towards Tyr86 (as it does the monosubstituted ring of *p*-coumaroyl aldehyde in AtDBR). The same steric hindrance is created by Phe291 in RiDBR (Fig. 7 C). The substitution of leucine (Leu289) with methionine (Met289) in RiDBR compared to MdDBR probably orients the phenol ring of 4-hydroxybenzalacetone (HBA) towards Tyr264 (Fig 7B and 7D).

Reaction mechanisms have been proposed for diverse DBRs, like AtDBR [8], guinea pig 12-HD/PGR [33] and rat liver AOR [12], in which the conjugated double bond of the substrate is in equilibrium with an α, β-conjugated enolate intermediate. In this condition, a hydride transfer occurs from the C4 atom of the nicotine amide of NADPH (catalytic carbon) to the β carbon of the enolate intermediate, with a subsequent protonation of its α carbon (Fig. 1). In AtDBR it has been suggested that this process is facilitated by the stabilization of the propenal transition state by a π-π interaction between Tyr-53 and the phenolic ring of the substrate [8]. In RiDBR ternary structure, a π-π stacking between the substrate HBA and nicotinamide aromatic rings is observed, with a hydride transfer distance of 3.06 Å to the alkene double bond [34]. In the MdDBR ternary structure described here, due to the different orientation of the ligand compared to the other structures superimposed, the propenal group of FER is too distant

from the nicotinamide ring of NADP(H) to justify a hydride transfer (7.08 Å), as it happens for NtDBR ternary structure [10]. It is plausible that in both MdDBR and NtDBR structures, due to the steric hindrances described, ligands bind to the enzyme in an orientation that does not allow the reaction to occur.

3.3 Enzymatic properties of MdDBR

The activity of purified MdDBR protein towards a variety of phenylpropanoid-like substrates was tested by *in vitro* assays (Table 3). Steady-state kinetic analyses were performed for **(a)** by monitoring NADPH oxidation at 365 nm on a UV/VIS scanning spectrophotometer (Table 2). Since all the other substrates strongly absorb between 250-450 nm, the spectrophotometric method was not compatible and therefore the conversion in the reduced products were monitored by UPLC-DAD analyses.

Among all the substrate tested, MdDBR showed activity only on **(a)**, **(b)** and (**f**), reducing the present alkenal double bond (Fig. 3S, Fig. 4S). The specific activity for *trans*-4-phenyl-3-buten-2-one **(a)** is here reported for the first time and it has a similar value as the one reported by Mansell et al. for NtDBR towards 1-nitrocyclohexene at pH 5.4 [10]. A substrate conversion in its hydrogenated product has been observed already after 15 minutes reaction for **(b)** (Fig. S3 B) and after 30 min for (**f**) (Fig. S4 B). For both assays the substrates and potential products (Fig. S3 A, Fig. S4 A) showed the same retention time range as the peaks identified in the extracts of the MdDBR assays. Furthermore, the DAD profiles of the substrates and products show a high overlap, leading to the identification of the enzymatic products. MdDBR does not catalyze the reduction of C=C of ferulic acid **(e)** and its ketonic homolog **(c)** (not shown). Most likely the 3-methoxy group prevents these compounds to go deeply in the active site cavity, possibly hindering the hydride transfer from NADPH.

MdDBR showed no evidence of activity against *p*-coumaric acid (**d**) (not shown). However, it can reduce the corresponding aldehyde (**f**) (Fig. 4S B). The activity of MdDBR towards 4-hydroxy substituted carbonyl compounds **(b)** and **(f)** is plausibly explained by the presence of a ketone for **(b)** and an aldehyde for **(f)** as compared to the carboxyl group of *p*-coumaric acid **(d)** that is not reduced.

Despite the low number of compounds tested, the presence of a ketone or an aldehyde group conjugated with the C=C it is likely to be fundamental for substrate activity in MdDBR. Furthermore, the presence of 3-methoxyl group in the aromatic ring may correlate with the absence of activity. MdDBR has been previously described as active towards *p*-coumaroyl-CoA and feruloyl-CoA [15]. Although we used the same experimental conditions and the same plasmid construct used by Ibdah *et al.* [15], we did not observe any conversion for these substrates.

3.4 Docking calculations

In order to build models of the ternary complex of MdDBR with compounds **a**-**f**, the structure of MdDBR binary complex was used. Compounds **g** and **h** were not considered in the calculations because of the large size as compared to the dimensions of the binding pocket. The structure of the ternary complex solved in this study was not used because of the disordered region (residues 68-73) in the proximity of the binding pocket and affecting the shape and the electrostatics of the binding pocket itself. For the same reason, it was not possible to follow the typical benchmark redocking procedure on the MdDBR and on the AtDBR (disordered residues: 61-69) ternary complex

structures. Docking calculations were performed using the OpenEye FRED 3.4.0.5 [28] software, belonging to OpenEye OEDocking 3.4.0.5 suite. The protein was prepared for the docking by using the OpenEye Make Receptor 3.5.0.4 tool. Make Receptor also add the missing hydrogen atoms by using an automatic procedure. The box defining the binding site was centered on the $NADP^+$ catalytic carbon and its dimensions were 18 x 21 x 21 Å.

The results of the docking calculations are reported in Fig. 8. All the compounds are located in the proximity of the $NADP^+$ ligand and form a H-bond between their carbonyl moiety and the $NADP^+$ hydroxyl group bound to ribose C2 atom. When a hydroxyl group is present on the aromatic ring (compounds **b-f**), a H-bond is formed also with the hydroxyl group of Tyr86 and in one case (compound **d**) also with Tyr294. In the case of compounds **a**, **b** and **f**, the carbon C7 is at ca. 3.5 – 3.8 Å from the $NADP^+$ catalytic carbon and the double bond is in a good alignment with the nitrogenous base. As confirmed by *in vitro* enzymatic assays, for these compounds MdDBR catalyzes the double bond reduction, most likely with the reaction mechanism proposed for AtDBR [9]. In the case of compounds **c** and **e**, where no substrate reduction has been observed in *in vitro* experiments, the distance between the ligand's double bond and the $NADP^+$ catalytic carbon is larger with respect to compounds **a**, **b** and **f**, and the molecules have been distorted during the docking (i.e. they are no more planar, as expected for molecules with conjugate double bonds). The distortion of compounds **c** and **e** can be a symptom of the fact that these molecules are not able to accommodate easily inside the binding pocket, this could be the reason why in the MdDBR ternary structure **e** binds the protein in a no active mode. Finally, in the case of compound **d** the orientation is similar to that of compounds **a**, **b** and **f**, but the distance between the double bond and the $NADP^+$ catalytic carbon is slightly larger (4.2 Å), which is consistent with a lower reactivity.

4. Conclusion

We report the crystal structures of the apo form, $NADP^+$ bound and $NADP^+$-FER bound form of MdDBR, as well as the characterization of its catalytic activities.

A structural comparison of the apo form and the ligand bound form of MdDBR demonstrates that binding of $NADP^+$ and FER induces a shift of key amino acids in the active site due to new interactions between the protein and the ligands. The superimposition of MdDBR structure with similar DBRs from other plant species indicates different orientations of the substrates in each protein, due to variations of substrate binding residues in the active site cleft. In particular, the role of MdDBR Leu289 and Phe291 has been highlighted. These diversities most probably influence the substrate specificity of each DBR.

The use of high-resolution structural data, together with docking calculations on the base of the structures solved, allowed the identification of important residues for substrate binding, interaction and catalysis; these results are crucial to drive site directed mutagenesis aimed at the improvement of MdDBR catalytic properties and to further expand the biocatalytic potential of this enzyme. Further investigations on substrate specificity of MdDBR as well as *in planta* studies are necessary to elucidate its role in the phenylpropanoid and previously proposed dihydrochalcone pathway. Based on the data obtained here it seems very unlikely that MdDBR is the key enzyme in the synthesis of dihydrochalcones in apples.

Acknowledgements:

The research leading to these results has received funding from the Free University of Bolzano under the Euregio Interregional Project Network (IPN 55) - EXPOAPPLE2 – EXploring the POtential of APPLE dihydrochalcones on novel cosmetical, nutritional and pharmaceutical applications [GECT Euregio Tirolo-Alto Adige-Trentino", 2° call]. We thank ELETTRA Sincrotrone Trieste for beamtime under proposals 20200479 and 20180463.

[1] G. Forkmann, S. Martens, Metabolic engineering and applications of flavonoids, Curr. Opin. Biotechnol. 12 (2001) 155–160. https://doi.org/10.1016/S0958-1669(00)00192-0.

[2] Y. Deng, S. Lu, Biosynthesis and Regulation of Phenylpropanoids in Plants, CRC. Crit. Rev. Plant Sci. 36 (2017) 257–290. https://doi.org/10.1080/07352689.2017.1402852.

[3] M. Karonen, M. Hämäläinen, R. Nieminen, K.D. Klika, J. Loponen, V. V. Ovcharenko, E. Moilanen, K. Pihlaja, Phenolic extractives from the bark of Pinus sylvestris L. and their effects on inflammatory mediators nitric oxide and prostaglandin E 2, J. Agric. Food Chem. 52 (2004) 7532–7540. https://doi.org/10.1021/jf048948q.

[4] M. Ibdah, S. Martens, D.R. Gang, Biosynthetic Pathway and Metabolic Engineering of Plant Dihydrochalcones, J. Agric. Food Chem. 66 (2018) 2273–2280. https://doi.org/10.1021/acs.jafc.7b04445.

[5] J.R.L. Ehrenkranz, N.G. Lewis, C.R. Kahn, J. Roth, Phlorizin: A review, Diabetes. Metab. Res. Rev. 21 (2005) 31–38. https://doi.org/10.1002/dmrr.532.

[6] T. Min, H. Kasahara, D.L. Bedgar, B. Youn, P.K. Lawrence, D.R. Gang, S.C. Halls, H.J. Park, J.L. Hilsenbeck, L.B. Davin, N.G. Lewis, C.H. Kang, Crystal Structures of Pinoresinol-Lariciresinol and Phenylcoumaran Benzylic Ether Reductases and Their Relationship to Isoflavone Reductases, J. Biol. Chem. 278 (2003) 50714–50723. https://doi.org/10.1074/jbc.M308493200.

[7] Q.-H. Ma, Functional analysis of a cinnamyl alcohol dehydrogenase involved in lignin biosynthesis in wheat, J. Exp. Bot. 61 (2010) 2735–2744. https://doi.org/10.1093/jxb/erq107.

[8] B. Youn, S.G.A. Moinuddin, L.B. Davin, N.G. Lewis, C. Kang, Crystal structures of apo-form and binary/ternary complexes of Podophyllum secoisolariciresinol dehydrogenase, an enzyme involved in formation of health-protecting and plant defense lignans, J. Biol. Chem. 280 (2005) 12917–12926. https://doi.org/10.1074/jbc.M413266200.

[9] B. Youn, S.J. Kim, S.G. A, C. Lee, D.L. Bedgar, A.R. Harper, L.B. Davin, N.G. Lewis, C.H. Kang, B. Youn, S.J. Kim, S.G.A.A. Moinuddin, C. Lee, D.L. Bedgar, A.R. Harper, L.B. Davin, N.G. Lewis, C.H. Kang, S.G. A, C. Lee, D.L. Bedgar, A.R. Harper, L.B. Davin, N.G. Lewis, C.H. Kang, B. Youn, S.J. Kim, S.G.A.A. Moinuddin, C. Lee, D.L. Bedgar, A.R. Harper, L.B. Davin, N.G. Lewis, C.H. Kang, Mechanistic and structural studies of apoform, binary, and ternary complexes of the Arabidopsis alkenal double bond reductase At5g16970, J. Biol. Chem. 281 (2006) 40076–40088. https://doi.org/10.1074/jbc.M605900200.

[10] D.J. Mansell, H.S. Toogood, J. Waller, J.M.X.X. Hughes, C.W. Levy, J.M. Gardiner, N.S. Scrutton, Biocatalytic asymmetric alkene reduction: Crystal structure and characterization of a double bond reductase from Nicotiana tabacum, ACS Catal. 3 (2013) 370–379. https://doi.org/10.1021/cs300709m.

[11] R. Stuermer, B. Hauer, M. Hall, K. Faber, Asymmetric bioreduction of activated C=C bonds using enoate reductases from the old yellow enzyme family, Curr. Opin. Chem. Biol. 11 (2007) 203–213.

https://doi.org/10.1016/j.cbpa.2007.02.025.

[12] R.A. Dick, T.W. Kensler, The Catalytic and Kinetic Mechanisms of NADPH-dependent Alkenal/one Oxidoreductase, J. Biol. Chem. 279 (2004) 17269–17277. https://doi.org/10.1074/jbc.M400427200.

[13] H. Kasahara, Y. Jiao, D.L. Bedgar, S.J. Kim, A.M. Patten, Z.Q. Xia, L.B. Davin, N.G. Lewis, Pinus taeda phenylpropenal double-bond reductase: Purification, cDNA cloning, heterologous expression in Escherichia coli, and subcellular localization in P. taeda, Phytochemistry. 67 (2006) 1765–1780. https://doi.org/10.1016/j.phytochem.2006.07.001.

[14] T. Koeduka, B. Watanabe, S. Suzuki, J. Hiratake, J. Mano, K. Yazaki, Characterization of raspberry ketone/zingerone synthase, catalyzing the alpha, beta-hydrogenation of phenylbutenones in raspberry fruits, Biochem. Biophys. Res. Commun. 412 (2011) 104–108. https://doi.org/10.1016/j.bbrc.2011.07.052.

[15] M. Ibdah, A. Berim, S. Martens, A.L.H. Valderrama, L. Palmieri, E. Lewinsohn, D.R. Gang, Identification and cloning of an NADPH-dependent hydroxycinnamoyl-CoA double bond reductase involved in dihydrochalcone formation in Malus × domestica Borkh., Phytochemistry. 107 (2014) 24–31. https://doi.org/10.1016/j.phytochem.2014.07.027.

[16] J. Boyer, R.H. Liu, Apple phytochemicals and their health benefits, Nutr. J. 3 (2004) 1–15. https://doi.org/10.1186/1475-2891-3-5.

[17] F.W. Studier, Protein production by auto-induction in high density shaking cultures., Protein Expr. Purif. 41 (2005) 207–34. https://doi.org/10.1016/j.pep.2005.01.016.

[18] P. Artimo, M. Jonnalagedda, K. Arnold, D. Baratin, G. Csardi, E. De Castro, S. Duvaud, V. Flegel, A. Fortier, E. Gasteiger, A. Grosdidier, C. Hernandez, V. Ioannidis, D. Kuznetsov, R. Liechti, S. Moretti, K. Mostaguir, N. Redaschi, G. Rossier, I. Xenarios, H. Stockinger, ExPASy: SIB bioinformatics resource portal, Nucleic Acids Res. 40 (2012). https://doi.org/10.1093/nar/gks400.

[19] A. Lausi, M. Polentarutti, S. Onesti, J.R. Plaisier, E. Busetto, G. Bais, L. Barba, A. Cassetta, G. Campi, D. Lamba, A. Pifferi, S.C. Mande, D.D. Sarma, S.M. Sharma, G. Paolucci, Status of the crystallography beamlines at Elettra, Eur. Phys. J. Plus. 130 (2015) 1–8. https://doi.org/10.1140/epjp/i2015-15043-3.

[20] W. Kabsch, Integration, scaling, space-group assignment and post-refinement, Acta Crystallogr. Sect. D Biol. Crystallogr. 66 (2010) 133–144. https://doi.org/10.1107/S0907444909047374.

[21] M.D. Winn, C.C. Ballard, K.D. Cowtan, E.J. Dodson, P. Emsley, P.R. Evans, R.M. Keegan, E.B. Krissinel, A.G.W. Leslie, A. McCoy, S.J. McNicholas, G.N. Murshudov, N.S. Pannu, E.A. Potterton, H.R. Powell, R.J. Read, A. Vagin, K.S. Wilson, Overview of the CCP4 suite and current developments, Acta Crystallogr. Sect. D Biol. Crystallogr. 67 (2011) 235–242. https://doi.org/10.1107/S0907444910045749.

[22] A. Vagin, A. Teplyakov, Molecular replacement with MOLREP, Acta Crystallogr. Sect. D Biol. Crystallogr.

66 (2010) 22–25. https://doi.org/10.1107/S0907444909042589.

[23] G.N. Murshudov, P. Skubák, A.A. Lebedev, N.S. Pannu, R.A. Steiner, R.A. Nicholls, M.D. Winn, F. Long, A.A. Vagin, REFMAC5 for the refinement of macromolecular crystal structures, Acta Crystallogr. Sect. D Biol. Crystallogr. 67 (2011) 355–367. https://doi.org/10.1107/S0907444911001314.

[24] P. Emsley, B. Lohkamp, W.G. Scott, K. Cowtan, Features and development of Coot, Acta Crystallogr. Sect. D Biol. Crystallogr. 66 (2010) 486–501. https://doi.org/10.1107/S0907444910007493.

[25] E.F. Pettersen, T.D. Goddard, C.C. Huang, G.S. Couch, D.M. Greenblatt, E.C. Meng, T.E. Ferrin, UCSF Chimera - A visualization system for exploratory research and analysis, J. Comput. Chem. 25 (2004) 1605–1612. https://doi.org/10.1002/jcc.20084.

[26] J. Wang, R.M. Wolf, J.W. Caldwell, P.A. Kollman, D.A. Case, Development and testing of a general Amber force field, J. Comput. Chem. 25 (2004) 1157–1174. https://doi.org/10.1002/jcc.20035.

[27] P.C.D. Hawkins, A.G. Skillman, G.L. Warren, B.A. Ellingson, M.T. Stahl, Conformer generation with OMEGA: Algorithm and validation using high quality structures from the protein databank and cambridge structural database, J. Chem. Inf. Model. 50 (2010) 572–584. https://doi.org/10.1021/ci100031x.

[28] M. McGann, FRED pose prediction and virtual screening accuracy, J. Chem. Inf. Model. 51 (2011) 578–596. https://doi.org/10.1021/ci100436p.

[29] E. Krissinel, K. Henrick, Secondary-structure matching (SSM), a new tool for fast protein structure alignment in three dimensions, Acta Crystallogr. Sect. D Biol. Crystallogr. 60 (2004) 2256–2268. https://doi.org/10.1107/S0907444904026460.

[30] H. Riveros-Rosas, A. Julián-Sánchez, R. Villalobos-Molina, J.P. Pardo, E. Piña, Diversity, taxonomy and evolution of medium-chain dehydrogenase/reductase superfamily, Eur. J. Biochem. 270 (2003) 3309–3334. https://doi.org/10.1046/j.1432-1033.2003.03704.x.

[31] B. Persson, J. Hedlund, H. Jörnvall, Medium- and short-chain dehydrogenase/reductase gene and protein families: The MDR superfamily, Cell. Mol. Life Sci. 65 (2008) 3879–3894. https://doi.org/10.1007/s00018-008-8587-z.

[32] B. Youn, S. Kim, S.G. A, C. Lee, D.L. Bedgar, A.R. Harper, L.B. Davin, N.G. Lewis, C. Kang, B. Youn, S. Kim, S.G.A. Moinuddin, C. Lee, D.L. Bedgar, A.R. Harper, L.B. Davin, N.G. Lewis, C. Kang, Mechanistic and Structural Studies of Apoform , Binary , and Ternary Complexes of the Arabidopsis Alkenal Double Bond Reductase At5g16970 *, J. Biol. Chem. 281 (2006) 40076–40088. https://doi.org/10.1074/jbc.M605900200.

[33] T. Hori, T. Yokomizo, H. Ago, M. Sugahara, G. Ueno, M. Yamamoto, T. Kumasaka, T. Shimizu, M. Miyano, Structural basis of leukotriene B4 12-hydroxydehydrogenase/15-oxo-prostaglandin 13-reductase

catalytic mechanism and a possible Src homology 3 domain binding loop, J. Biol. Chem. 279 (2004) 22615–22623. https://doi.org/10.1074/jbc.M312655200.

[34] S.J. Moore, T. Tosi, Y.B. Hleba, D. Bell, K. Polizzi, P. Freemont, A cell-free synthetic biochemistry platform for raspberry ketone production, BioRxiv. (2017) 202341. https://doi.org/10.1101/202341.

[35] D. Liebschner, P. V. Afonine, N.W. Moriarty, B.K. Poon, O. V. Sobolev, T.C. Terwilliger, P.D. Adams, Polder maps: Improving OMIT maps by excluding bulk solvent, Acta Crystallogr. Sect. D Struct. Biol. 73 (2017) 148–157. https://doi.org/10.1107/S2059798316018210.

Table 1: Data collection and refinement statistics

Data collection	Apo -MdDBR	MdDBR-NADPH	MdDBR-NADP$^+$-FER
Wavelength (Å)	1.00	1.00	1.00
Resolution range (Å)	48.57-1.20 (1.22-1.20)	48.50 – 1.40 (1.42-1.40)	48.47–1.36 (1.39-1.36)
Temperature (K)	100	100	100
Space group	*C* 2	*I* 222	*I* 222
Unit cell parameters			
a, *b*, *c* (Å)	156.61, 68.67, 68.94	68.54, 68.64, 145.40	68.49, 68.61, 145.97
α, β, γ (°)	90, 111.38, 90	90, 90, 90	90, 90, 90
Mosaicity (°)	0.16	0.20	0.20
Total reflections	760122 (35901)	845118 (40398)	699440 (20877)
Unique reflections	210636 (10469)	67744 (3301)	72885 (3320)
Multiplicity	3.6 (3.4)	12.5 (12.2)	9.6 (6.3)
Completeness (%)	99.4 (99.9)	100 (100)	99.5 (89.7)
Mean I/sigma(I)	12.1 (2.3)	15.9 (1.1)	12.1 (0.9)
Wilson B factor (Å^2)	12.063	21.1	12.816
R_{merge}	0.044 (0.432)	0.076 (2.354)	0.087 (1.344)
R_{meas}	0.059 (0.584)	0.083 (2.568)	0.097 (1.584)
R_{pim}	0.039 (0.390)	0.032 (1.020)	0.042 (0.819)
$CC_{1/2}$	0.998 (0.784)	1 (0.517)	0.999 (0.493)
CC*	0.999 (0.937)	1 (0.993)	0.999 (0.812)
Reflection used in refinement	200156 (14893)	64352 (4669)	69315 (4728)
R-work	0.162 (0.239)	0.121 (0.383)	0.143 (0.517)
R-free	0.198 (0.285)	0.166 (0.389)	0.180 (0.578)
Number of non-hydrogen atoms	5798	3083	2908
Protein	5261	2729	2634
Ligands	10	65	74
Solvent	527	288	199
Sodium ions		1	1
Protein residues	678	351	340
RMS (bonds) (Å)	0.0188	0.015	0.017
RMS (angles) (°)	2.16	1.919	1.98
Ramachandran favored (%)	97.61	98	98.20
Ramachandran allowed (%)	1.94	1	1.2
Ramachandran outliers (%)	0.45	1	0
Rotamer outliers (%)	3.19	1.02	1.41
Clashscore	13.14	6.57	4.8
Avarage B-factor			
Protein	25.38	26.39	20.97
Ligands	23.83	24.21	19.83
Solvent	31.71	39.52	29.29
Sodium Ions		54.36	45.08

Highest resolution shell is shown in parentheses

Substrate	K_m	V_{max} (µkatal mg^{-1} prot)	K_{cat}
***Trans*-4 phenyl-3-buten-2-one (a)** 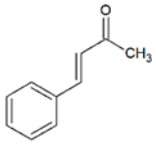	34.39 ± 4.26 µM	2.33 ± 0.097	5.83 ± 0.24 sec^{-1}

Table 2: Kinetic parameters of MdDBR with the substrate *Trans*-4 phenyl-3-buten-2-one

Substrate	MdDBR activity
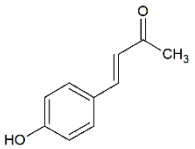 4-Hydroxybenzalacetone **(b)**	Substrate conversion to raspberry ketone
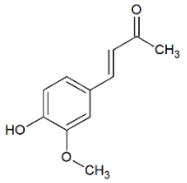 3-Methoxy-4-hydroxy-benzalacetone **(c)**	No activity
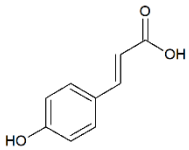 *p*-Coumaric acid **(d)**	No activity
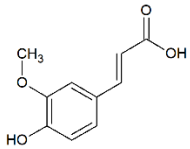 Ferulic acid **(e)**	No activity
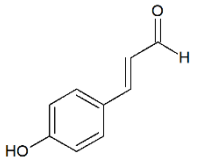 *p*-Coumaroyl aldehyde **(f)**	Substrate conversion to *p*-dihydrocoumaroyl aldehyde
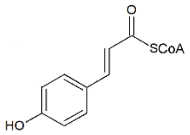 *p*-Coumaroyl CoA **(g)**	No activity
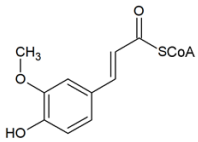 Feruloyl CoA **(h)**	No activity

Table 3. Substrates tested for determining MdDBR specificity.

Hydrogen bonds

	Monomer A residue	Dist. [Å]	Monomer B residue
1	A:GLU 270[OE1]	3.46	B:ARG 273[NH2]
2	A:CYS 272[O]	2.84	B:CYS 272[N]
3	A:GLN 282[OE1]	2.93	B:LEU 289[N]
4	A:VAL 283[O]	3.00	B:GLY 287[N]
5	A:MET 285[O]	2.82	B:MET 285[N]
6	A:LEU 289[O]	3.74	B:GLN 282[NE2]
7	A:CYS 272[N]	2.87	B:CYS 272[O]
8	A:SER 292[OG]	2.87	B:GLN 282[OE1]
9	A:GLY 287[N]	3.02	B:VAL 283[O]
10	A:MET 285[N]	2.81	B:MET 285[O]
11	A:GLN 282[NE2]	2.94	B:SER 292[OG]

Table S1: Predicted H-bond interactions forming the dimeric interface of MdDBR

Figure 1: Reaction mechanisms of the reduction of alkenal double bond catalysed by DBRs [12]

Figure 2: Structure of MdDBR apo in its crystallographic assembly (A), in complex with $NADP^+$ (B) and in complex with $NADP^+$ and FER (C). The substrate and the nucleotide binding domain are depicted in green and in yellow respectively. $NADP^+$ is shown in magenta, FER in blue.

Figure 3. Amino acid sequence alignment of MdDBR with AtDBR from *A. thaliana*, NtDBR from *N. tabacum* and RiDBR from *R. idaeus.* Secondary structure elements are represented on top: helices with squiggles, beta strands with arrows, turns with TT letters, conserved residues are written as white letters in red boxes. The dotted box highlights the nucleotide binding domain. Yellow bars indicate the conserved residues involved in NADP(H) binding.

Figure 4: Close-up view of MdDBR residues interacting with NADP(H) (A) and FER (B). The final (2|Fo|-|Fc|, φ) electron density map is contoured at 1.5σ and is shown in blue mesh. Carbon atoms are shown in magenta for $NADP^+$ and in blue for FER, nitrogen in blue, oxygen in red and sulfur in yellow. Selected key protein residues in the vicinity of the substrates are colored in grey and labeled. Water molecules are shown as red spheres, hydrogen bonds are shown as dotted lines.

Figure 5: Superposition of the substrates binding pocket of the three structure: MdDBR APO (gray), MdDBR in complex with $NADP^+$ (magenta) and MdDBR in complex with $NADP^+$ and FER (blue). Only residues showing a different orientation in the three structures are shown.

Figure 6: Superimposition of the active site residues plus ligands of the ternary structures of MdDBR (in blue and blue labels), *N. tabacum* DBR (NtDBR + NADPH + 4-hydroxy-3-methoxycinnamaldehyde (HMCA) PBD 4HFN) in yellow and yellow labels, *R. idaeus* ZS1 (RiDBR + NADPH + 4-hydroxybenzalacetone (HBA) PDB 6EOW) in pink and pink labels and *A. thaliana* DBR (AtDBR + NADPH + *p*-coumaroyl aldehyde, which is wrongly indicated as HC4 in the PDB 2J3J) in grey and black labels. Oxygen atoms are colored in red, nitrogen in blue and sulfur in yellow.

Figure 7: Surface representation of the active site cavity of AtDBR in complex with HC4 (PDB 2J3J) (A), of MdDBR in complex with FER (B) and of RiDBR in complex with HBA (PDB 6EOW) (C and D). FER has been added to the figure A and C as superposed ligand taken from MdDBR ternary structure. In the structures in figure B and D, HC4, belonging to AtDBR ternary structure, has been superposed. According to PDBeFOLD, the global RMSD between Cα-carbons is equal to 0.84 Å for AtDBR and MdDBR superposition, 0.56 Å for MdDBR and RiDBR superposition and 0.79 Å for RiDBR and AtDBR superposition. Carbon atoms are colored in white for AtDBR structure, in blue for MdDBR structure and in pink for RiDBR structure, oxygen atoms are colored in red,

nitrogen in blue and sulfur in yellow. For each different structure surface colors are the same as atom colors. Ligands have the same colors as the carbon atoms of the structure they belong to.

Figure 8: Result of the docking calculations performed on MdDBR. Panels A-F report the results for compounds **a-f**, respectively. The protein backbone is in ribbons representation, while the $NADP^+$ molecule and the residue involved in the binding of each ligand are in sticks colored according to the atom type. The hydrogen atoms have been hidden for readability. The hydrogen bonds between the protein and the ligand are reported using dashed red lines, while selected distances in Armstrong between the $NADP^+$ catalytic carbon and the ligand have been indicated using black dashed lines.

Figure S1: structure of the biological MdDBR homodimer predicted by PISA [29] and conserved in other DBRs [9]. Each monomer is differently colored (green or cyan). The residues of each monomer involved in the dimer interface are colored in red.

Figure S2: Polder electron density map calculated with exclusion of ferulic acid (FER). Polder map [35] is contoured at 4.5 rmsd, carve is 1.25. Map is shown in green mesh. Carbon atoms are shown in magenta for $NADP^+$ and in grey for the selected key protein residues in the vicinity of the substrates, nitrogen is in blue, oxygen in red and sulfur in yellow. Water molecules are shown as red spheres.

Figure S3: UPLC-DAD profile of DBR assay using 4-hydroxybenzalacetone as substrate. A: standards for 4-hydroxybenzalacetone and raspberry ketone; B: extract of enzyme assay; C: DAD profile of 4-hydroxybenzalacetone compared with peak S; D: DAD profile of raspberry ketone compared with peak P. S – substrate; P – product.

Figure S4: UPLC-DAD profile of DBR assay using *p*-coumaroyl aldehyde as substrate. A: standards for *p*-coumaroyl aldehyde and *p*-dihydrocoumaroyl aldehyde; B: extract of enzyme assay; C: DAD profile of *p*-coumaroyl aldehyde compared with peak S; D: DAD profile of *p*-dihydrocoumaroyl aldehyde compared with peak P. S – substrate; P – product.

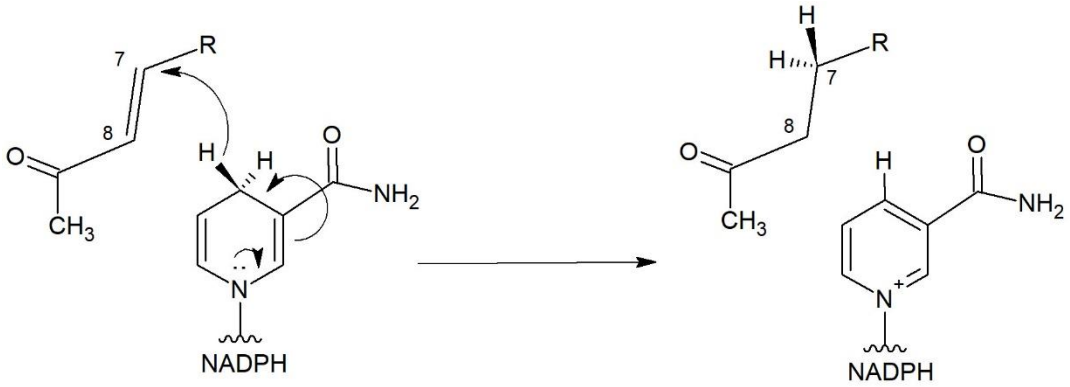

International Journal of Biological Macromolecules, Rosanna Caliandro, Ivan Polsinelli, Nicola Demitri, Francesco Musiani, Stefan Martens, Stefano Benini. Figure 1

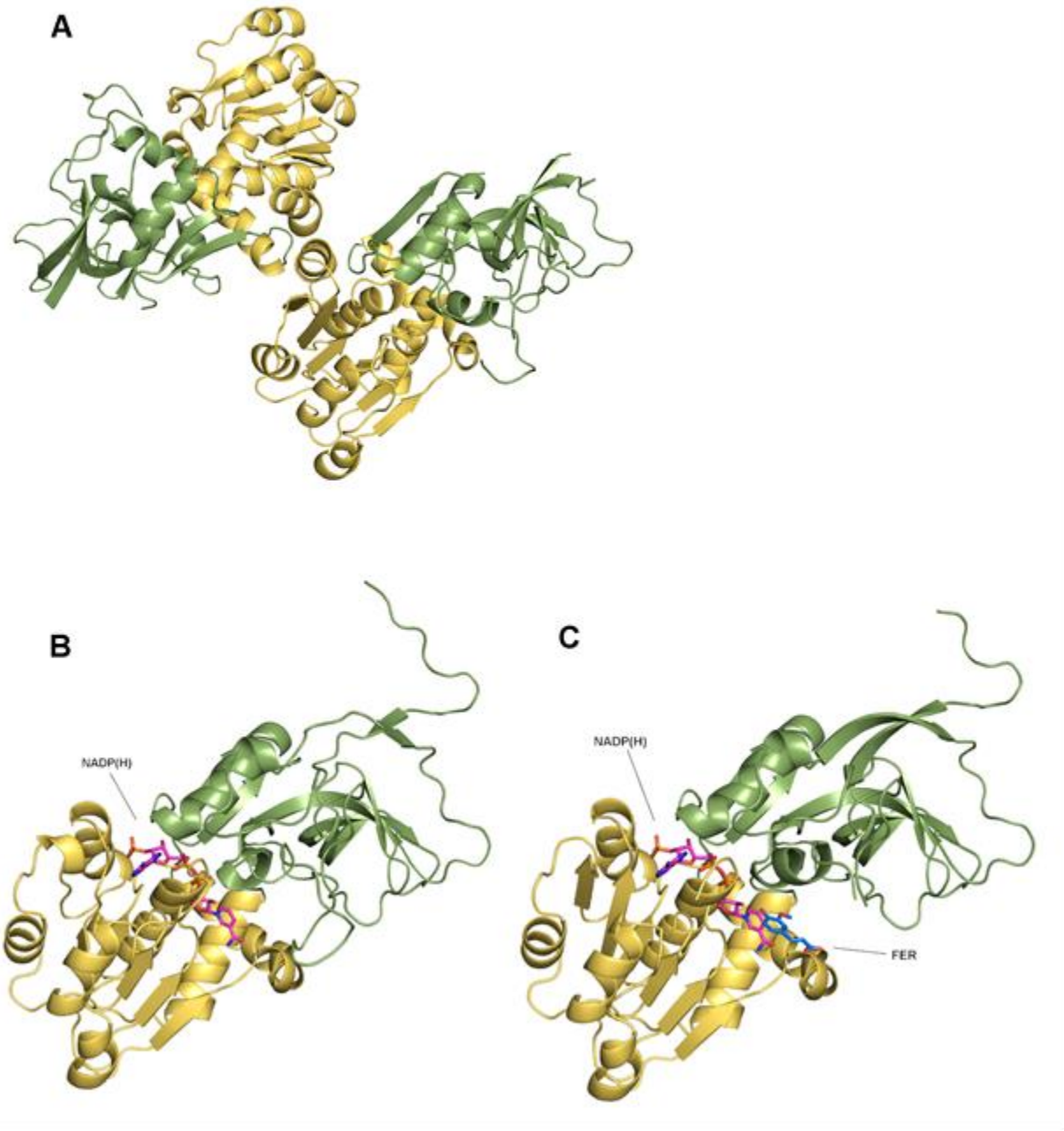

International Journal of Biological Macromolecules, Rosanna Caliandro, Ivan Polsinelli, Nicola Demitri, Francesco Musiani, Stefan Martens, Stefano Benini. Figure 2

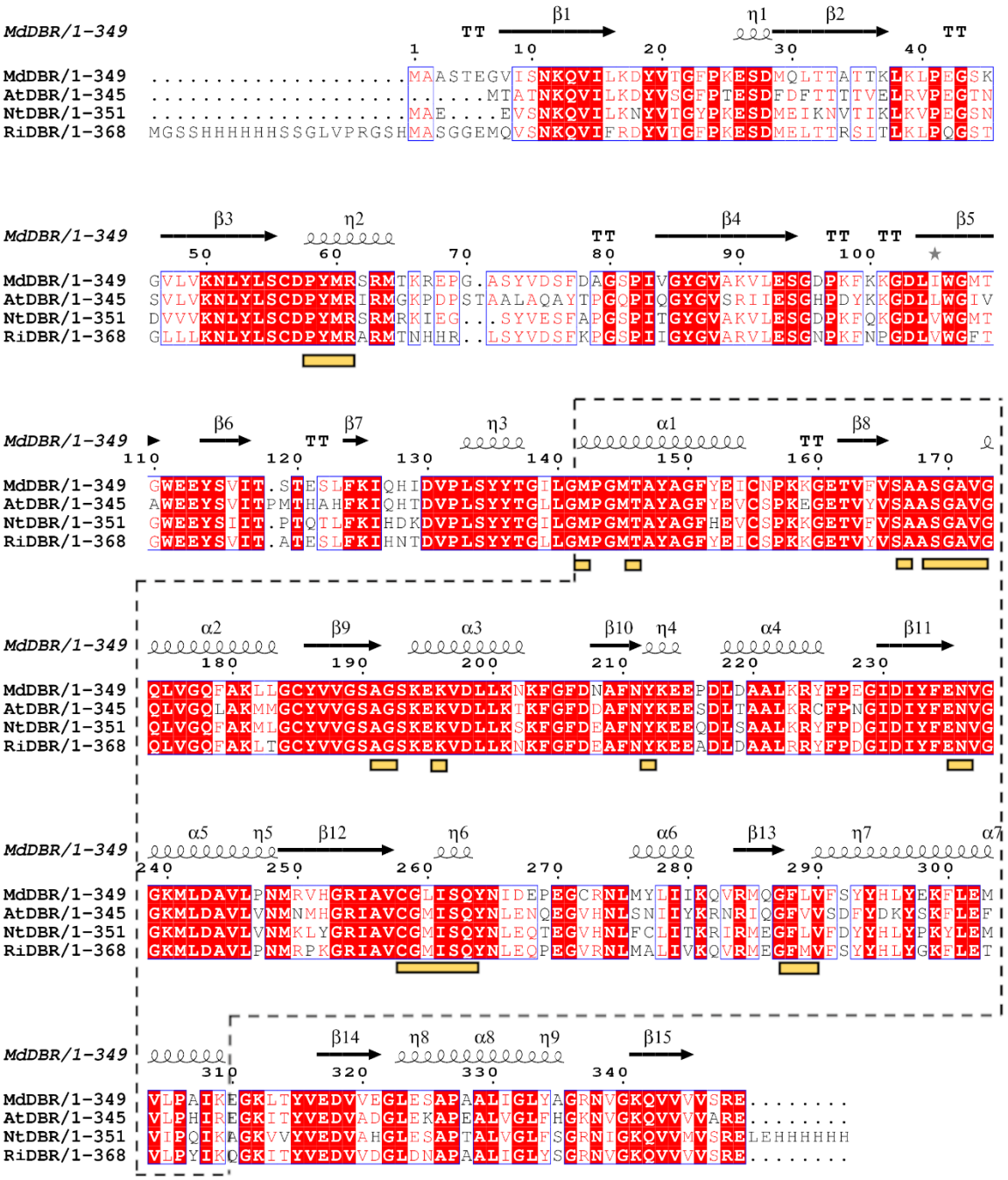

International Journal of Biological Macromolecules, Rosanna Caliandro, Ivan Polsinelli, Nicola Demitri, Francesco Musiani, Stefan Martens, Stefano Benini. Figure 3

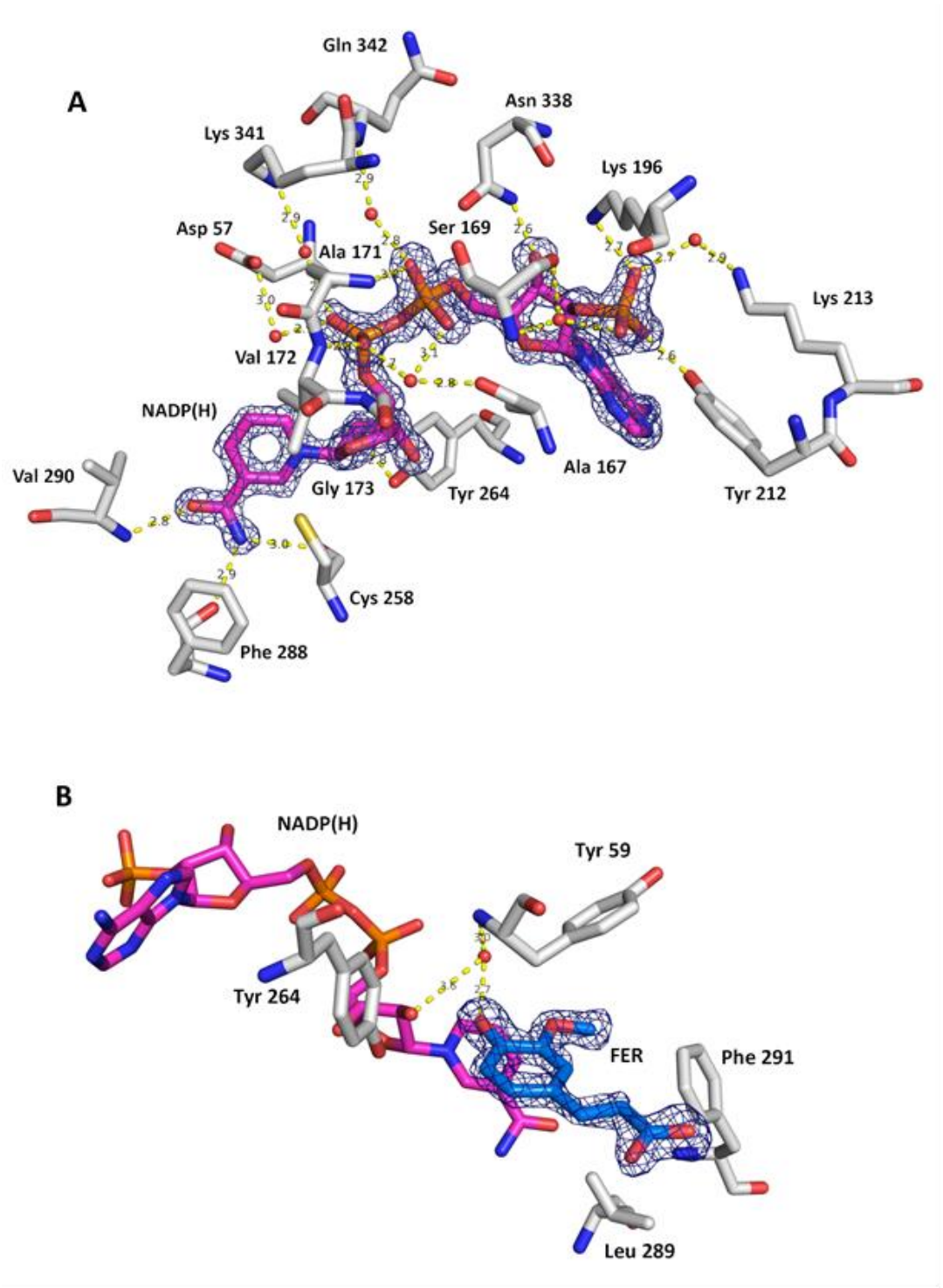

International Journal of Biological Macromolecules, Rosanna Caliandro, Ivan Polsinelli, Nicola Demitri, Francesco Musiani, Stefan Martens, Stefano Benini. Figure 4

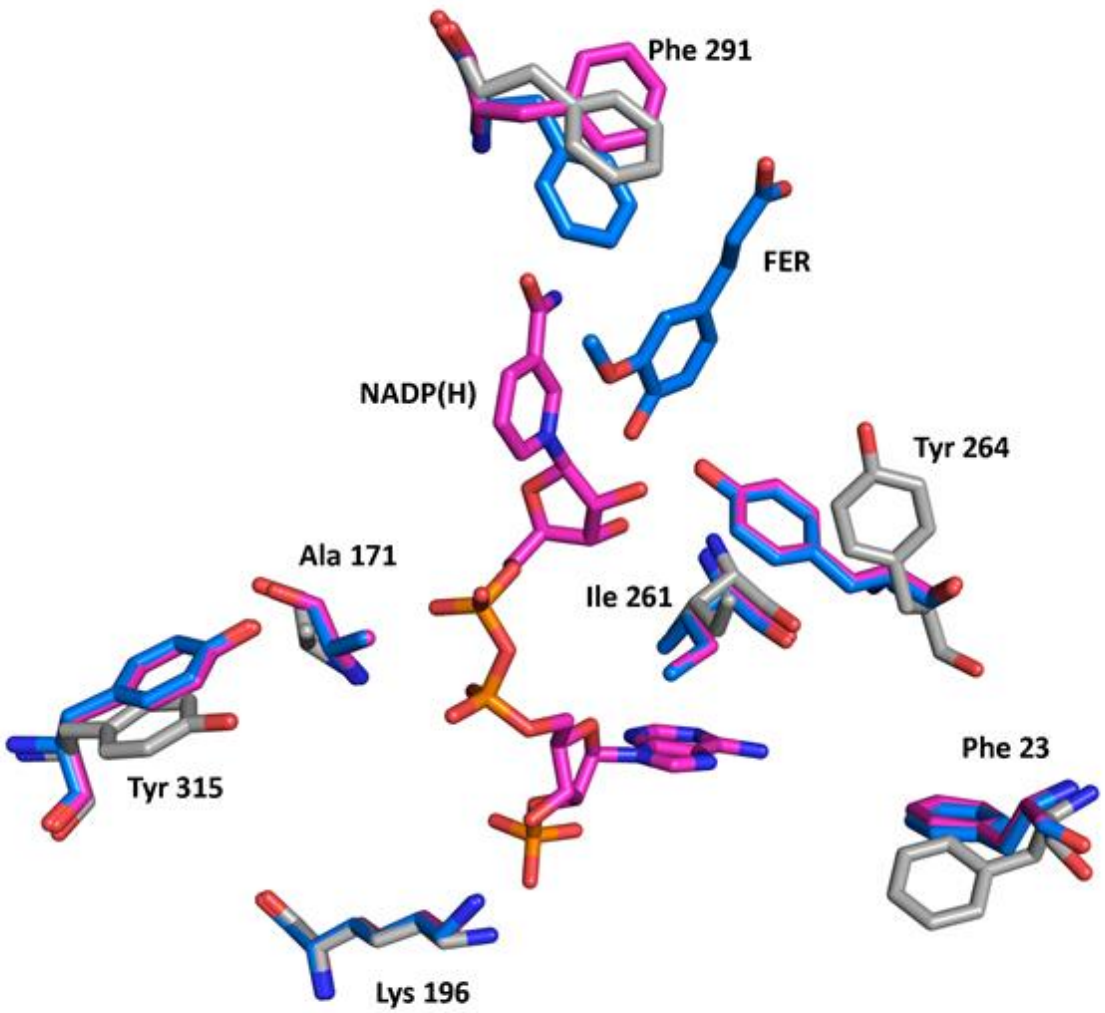

International Journal of Biological Macromolecules, Rosanna Caliandro, Ivan Polsinelli, Nicola Demitri, Francesco Musiani, Stefan Martens, Stefano Benini. Figure 5

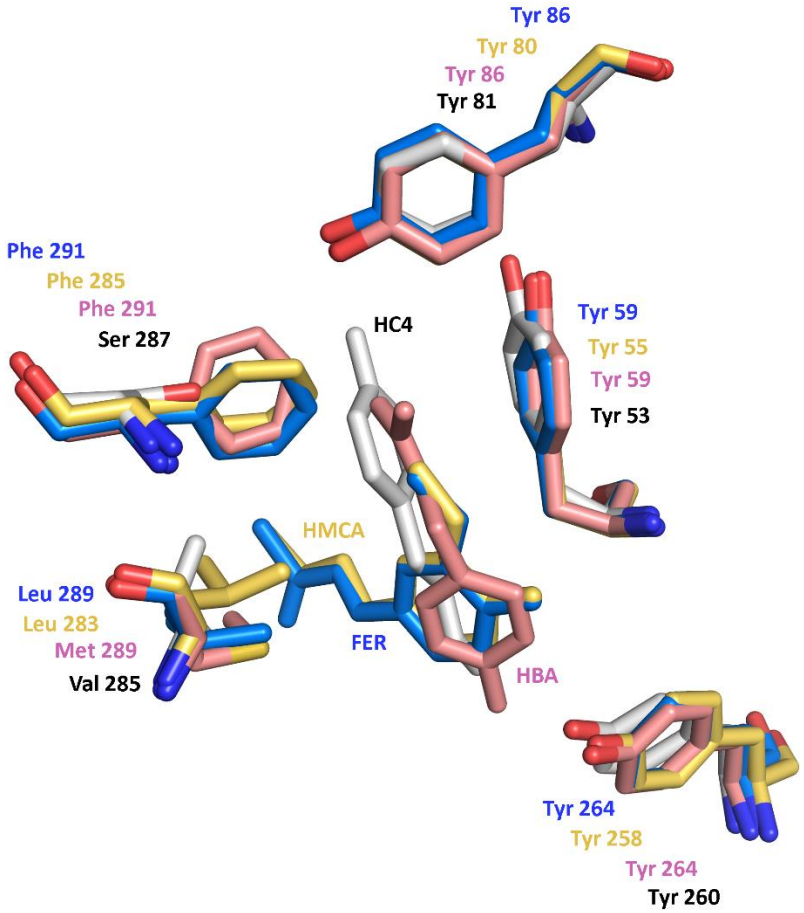

International Journal of Biological Macromolecules, Rosanna Caliandro, Ivan Polsinelli, Nicola Demitri, Francesco Musiani, Stefan Martens, Stefano Benini. Figure 6

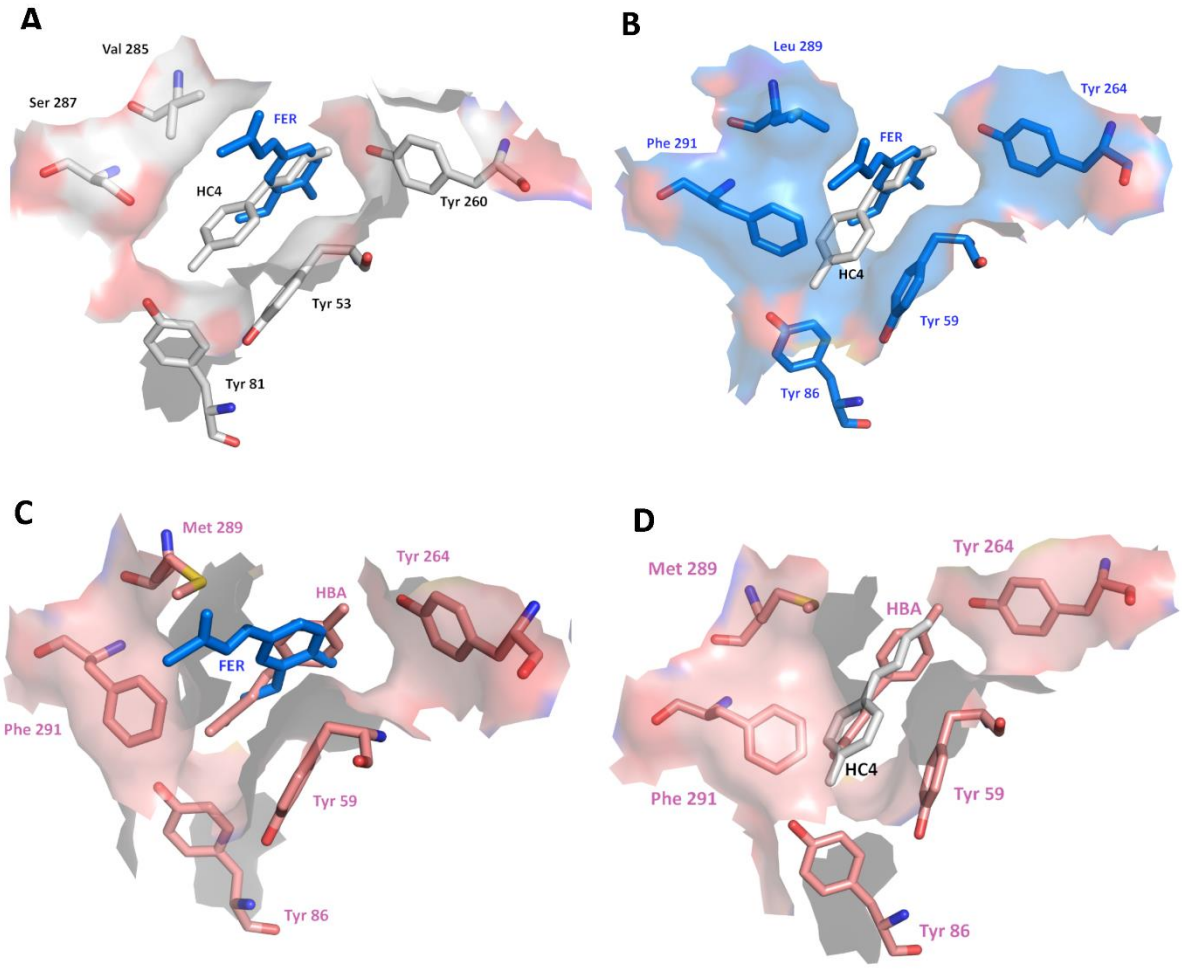

International Journal of Biological Macromolecules, Rosanna Caliandro, Ivan Polsinelli, Nicola Demitri, Francesco Musiani, Stefan Martens, Stefano Benini. Figure 7

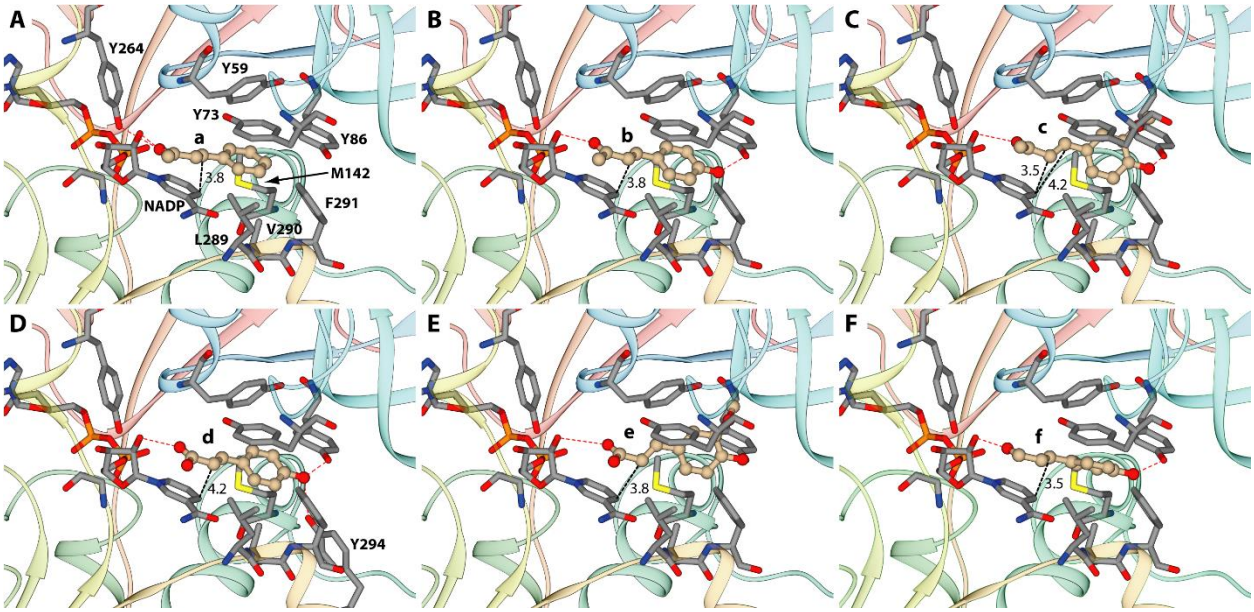

International Journal of Biological Macromolecules, Rosanna Caliandro, Ivan Polsinelli, Nicola Demitri, Francesco Musiani, Stefan Martens, Stefano Benini. Figure 8

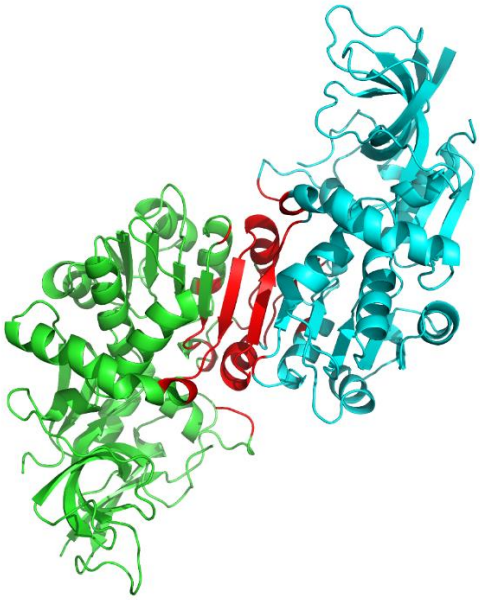

International Journal of Biological Macromolecules, Rosanna Caliandro, Ivan Polsinelli, Nicola Demitri, Francesco Musiani, Stefan Martens, Stefano Benini. Figure S1

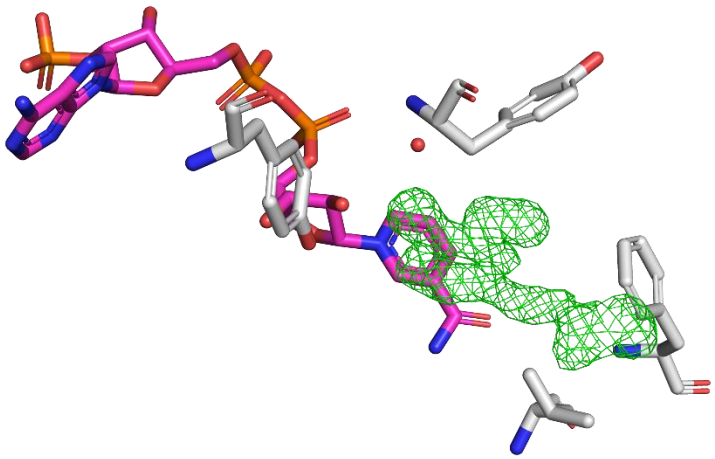

International Journal of Biological Macromolecules, Rosanna Caliandro, Ivan Polsinelli, Nicola Demitri, Francesco Musiani, Stefan Martens, Stefano Benini. Figure S2

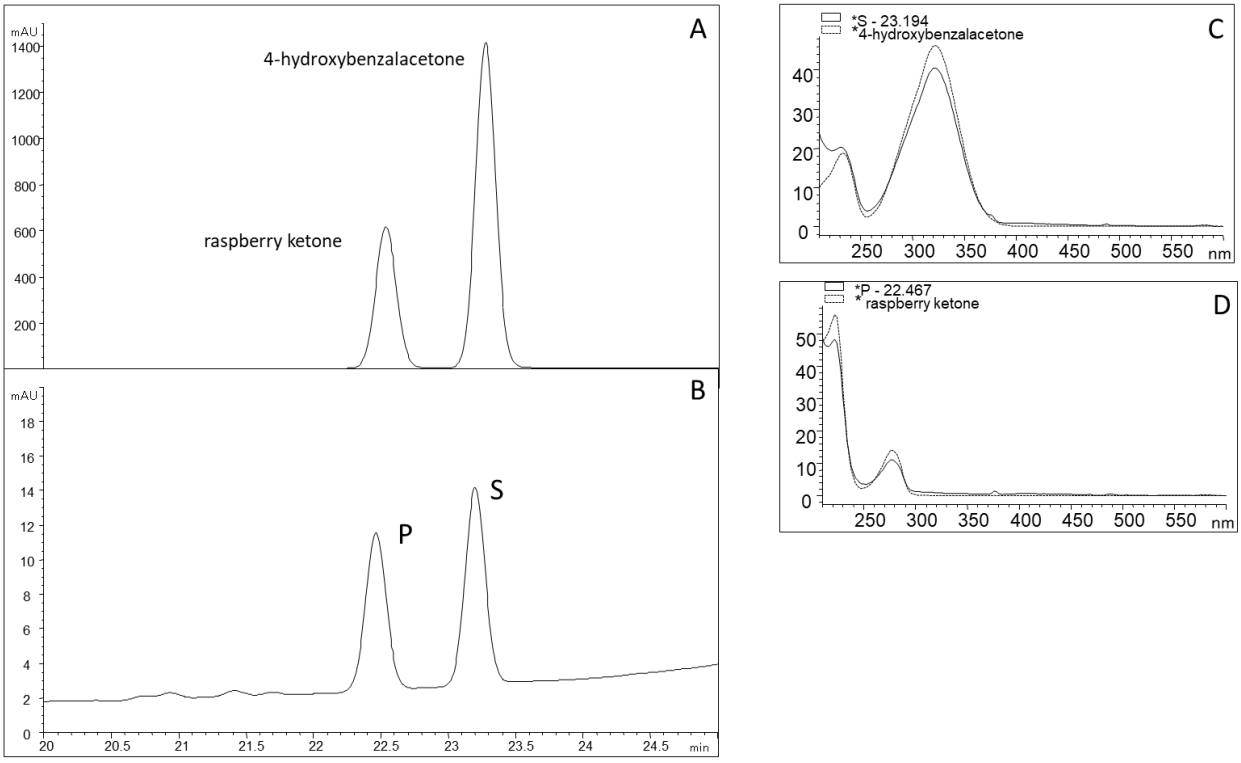

International Journal of Biological Macromolecules, Rosanna Caliandro, Ivan Polsinelli, Nicola Demitri, Francesco Musiani, Stefan Martens, Stefano Benini. Figure S3

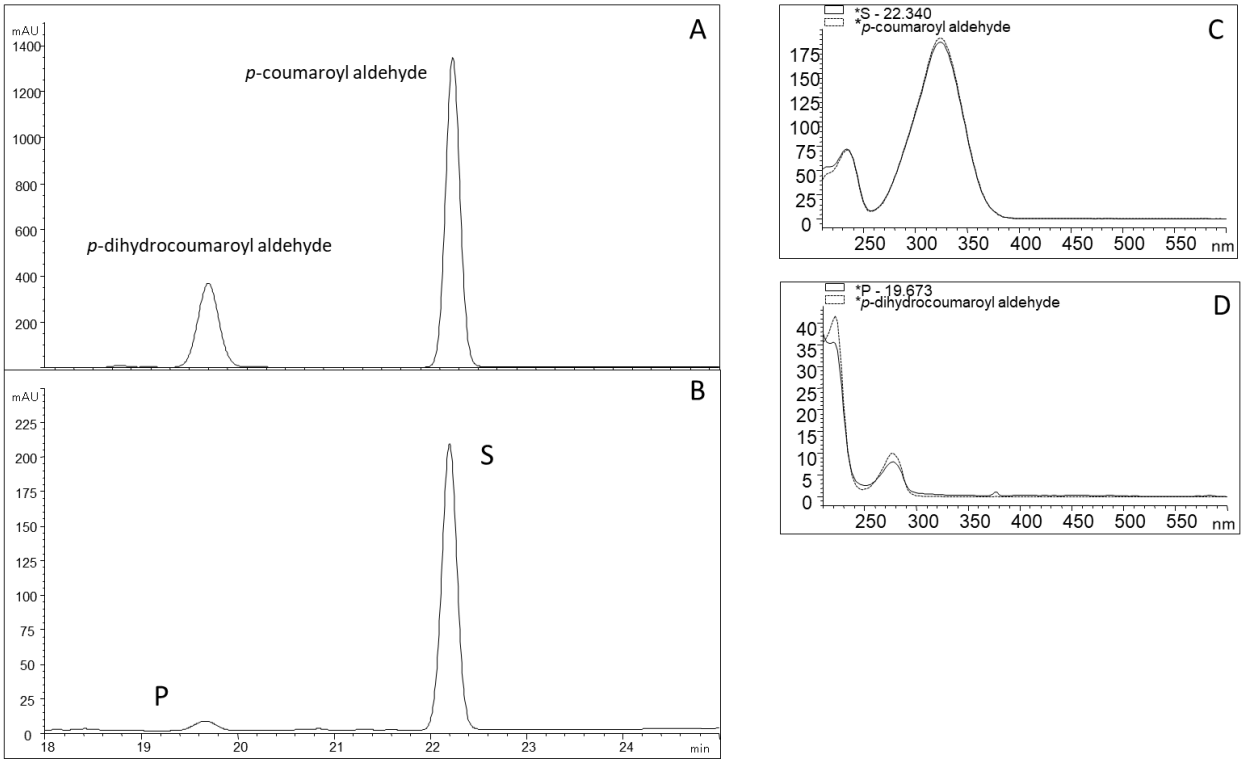

International Journal of Biological Macromolecules, Rosanna Caliandro, Ivan Polsinelli, Nicola Demitri, Francesco Musiani, Stefan Martens, Stefano Benini. Figure S4